

Solving Inverse Problems using Diffusion with Fast Iterative Renoising

Matt C. Bendel, Saurav K. Shastri, Rizwan Ahmad, and Philip Schniter
The Ohio State University, Columbus, OH, USA

bendel.8@osu.edu, shastri.19@osu.edu, rizwan.ahmad@osumc.edu, schniter.1@osu.edu

Abstract

Imaging inverse problems can be solved in an unsupervised manner using pre-trained diffusion models. In most cases, that involves approximating the gradient of the measurement-conditional score function in the reverse process. Since the approximations produced by existing methods are quite poor, especially early in the reverse process, we propose a new approach that re-estimates and “renoises” the image several times per diffusion step. Renoising aims to ensure that the pre-trained diffusion model sees white-Gaussian error, in accordance with how it was trained. We demonstrate the effectiveness of our “DDfire” method at 20, 100, and 1000 neural function evaluations on linear inverse problems and phase retrieval.

1. Introduction

Diffusion modeling has emerged as a powerful approach to generate samples from a complex distribution p_0 [21, 38, 39, 41, 42]. Recently, diffusion has also been used to solve inverse problems (see the survey [10]), where the goal is to recover $\mathbf{x}_0 \sim p_0$ from incomplete, distorted, and/or noisy measurements \mathbf{y} . The methodology is “unsupervised,” in that a diffusion model is trained to generate samples from p_0 and, at test time, the reverse process is modified to incorporate knowledge of the measurements \mathbf{y} , with the goal of sampling from the posterior distribution $p(\mathbf{x}_0|\mathbf{y})$.

A key challenge in the reverse process is approximating the conditional score $\nabla_{\mathbf{x}} \ln p_t(\mathbf{x}_t|\mathbf{y})$ at each step t , where \mathbf{x}_t is a additive-white-Gaussian-noise (AWGN) corrupted and possibly scaled version of $\mathbf{x}_0 \in \mathcal{X}^d$, and $\mathbf{y} \in \mathcal{Y}^m$ is treated as a draw from an assumed likelihood function $p(\mathbf{y}|\mathbf{x}_0)$. (Additional details will be given in Section 2.) Many existing approaches fall into one of two categories. The first writes $\nabla_{\mathbf{x}} \ln p_t(\mathbf{x}_t|\mathbf{y}) = \nabla_{\mathbf{x}} \ln p_t(\mathbf{x}_t) + \nabla_{\mathbf{x}} \ln p_t(\mathbf{y}|\mathbf{x}_t)$, where an approximation of $\nabla_{\mathbf{x}} \ln p_t(\mathbf{x}_t)$ is readily available from the p_0 -trained diffusion model, and then approximates $\nabla_{\mathbf{x}} \ln p_t(\mathbf{y}|\mathbf{x}_t)$ (e.g., [7, 40]). The second approach uses Tweedie’s formula [15] to write $\nabla_{\mathbf{x}} \ln p_t(\mathbf{x}_t|\mathbf{y})$ as an affine function of the con-

ditional denoiser $E\{\mathbf{x}_0|\mathbf{x}_t, \mathbf{y}\}$ (see (4)), and then approximates that denoiser (e.g., [9, 24, 43, 45]).

A key shortcoming of the aforementioned approaches is that their conditional-score approximations are not very accurate, especially early in the reverse process. For the methods that approximate $E\{\mathbf{x}_0|\mathbf{x}_t, \mathbf{y}\}$, we can assess the approximation quality both visually and via PSNR, since the exact $E\{\mathbf{x}_0|\mathbf{x}_t, \mathbf{y}\}$ maximizes PSNR given \mathbf{x}_t and \mathbf{y} . For the methods that approximate $\nabla_{\mathbf{x}} \ln p_t(\mathbf{x}_t|\mathbf{y})$, we can compute their equivalent approximations of $E\{\mathbf{x}_0|\mathbf{x}_t, \mathbf{y}\}$ using Tweedie’s rule:

$$E\{\mathbf{x}_0|\mathbf{x}_t, \mathbf{y}\} = \frac{\mathbf{x}_t + (1 - \bar{\alpha}_t) \nabla_{\mathbf{x}} \ln p_t(\mathbf{x}_t|\mathbf{y})}{\sqrt{\bar{\alpha}_t}}. \quad (1)$$

Figure S1 shows $E\{\mathbf{x}_0|\mathbf{x}_t, \mathbf{y}\}$ -approximations from the DDRM [24], DiffPIR [45], and DPS [7] solvers at different times in the reverse process for noiseless $4\times$ -super-resolution. The approximations show unwanted artifacts and oversmoothing, especially early in the reverse process. (See Figure S1 for an inpainting example.)

We thus seek an efficient way to improve the approximation of $E\{\mathbf{x}_0|\mathbf{x}_t, \mathbf{y}\}$ at each step t . We take inspiration from approximate message passing (AMP) [2, 14, 18, 34] for linear inverse problems, where $\mathbf{y} = \mathbf{A}\mathbf{x}_0 + \mathbf{w}$ for known \mathbf{A} and AWGN \mathbf{w} . AMP iterates between unconditional denoising and linear estimation from \mathbf{y} . When used with a large random \mathbf{A} , the distinguishing feature of AMP is that it presents the denoiser with additive white Gaussian noise (AWGN) at each iteration. This precisely matches how most denoisers (especially diffusion denoisers [21, 39]) are trained. With large random \mathbf{A} and mean-squared-error (MSE)-optimal denoising, AMP converges exponentially fast to the conditional-mean estimate $E\{\mathbf{x}_0|\mathbf{y}\}$. But with the structured \mathbf{A} that manifests in, e.g., inpainting, deblurring, and super-resolution, AMP performs poorly.

In this paper, we propose an iterative approach to approximating $E\{\mathbf{x}_0|\mathbf{x}_t, \mathbf{y}\}$, called Fast Iterative Renoising (FIRE). Like AMP, FIRE iterates unconditional denoising with linear estimation from \mathbf{y} . But unlike AMP, FIRE achieves AGWN-like denoiser input error by *renoising*, i.e., adding appropriately colored noise to the linear-estimation



Figure 1. Left column: True x_0 , noiseless $4\times$ -super-resolution y , and 50-iteration FIRE approximation of $E\{x_0|y\}$. Other columns: Approximations of $E\{x_0|x_t, y\}$ at different t (as measured by % NFEs). Note the over-smoothing with DDRM, DiffPIR, and DPS. For example, the mole on the subject’s forehead, visible in both x_0 and y , is missing from all DDRM, DiffPIR, and DPS images.

output, and works with any A . Figure 1 shows the 50-iteration FIRE approximation to $E\{x_0|x_T, y\} = E\{x_0|y\}$, which is relatively free of artifacts. Our proposed “DDfire” approach is then obtained by using FIRE in the denoising diffusion implicit model (DDIM) [39] reverse process. Figure 1 shows examples of DDfire’s $E\{x_0|x_t, y\}$ approximation when configured to run with 20, 100, and 1000 neural function evaluations (NFEs). DDfire’s $E\{x_0|x_t, y\}$ approximations have fewer structural artifacts and higher PSNR than its competitors at equal NFEs.

The contributions of this work are as follows:

1. For AWGN-corrupted linear inverse problems, we propose a diffusion sampler based on Fast Iterative RENOising (FIRE), which we call “DDfire.”
2. For generalized linear inverse problems, we propose an extension of DDfire inspired by expectation propagation.
3. We demonstrate advantages over several existing diffusion samplers on box inpainting, Gaussian and motion blur, super-resolution, and phase retrieval, in both recovery accuracy and runtime.

2. Background

Diffusion models corrupt training data from p_0 with ever-increasing amounts of noise, and then learn to reverse this process in a way that can generate samples from p_0 .

The popular “variance preserving” (VP) incarnation of diffusion [42] writes the forward process as a stochastic differential equation (SDE) $dx = -\frac{1}{2}\beta(t)x dt + \sqrt{\beta(t)} dw$ over t from 0 to T , where $\beta(t)$ is a variance schedule and dw is the standard Wiener process (SWP). The corresponding reverse process runs the SDE $dx = [-\frac{1}{2}\beta(t)x -$

$\beta(t)\nabla_x \ln p_t(x)] dt + \sqrt{\beta(t)} d\bar{w}$ backwards over t from T to 0, where $p_t(\cdot)$ is the marginal distribution of x at t and $d\bar{w}$ is the SWP run backwards. The “score” $\nabla_x \ln p_t(x)$ can be approximated using a deep neural network (DNN) $s_\theta(x, t)$ trained via denoising score matching [22].

In DDPM [21], the SDEs are discretized at $t \in \{0, 1, \dots, T\}$, yielding the VP forward process $x_t = \sqrt{1 - \beta_t}x_{t-1} + \sqrt{\beta_t}w_{t-1}$ with i.i.d $w_t \sim \mathcal{N}(0, I)$. This implies, using $\alpha_t \triangleq 1 - \beta_t$ and $\bar{\alpha}_t \triangleq \prod_{s=1}^t \alpha_s$, that

$$x_t = \sqrt{\bar{\alpha}_t}x_0 + \sqrt{1 - \bar{\alpha}_t}\epsilon_t, \quad \epsilon_t \sim \mathcal{N}(0, I). \quad (2)$$

The DDPM reverse process uses $\sigma_t^2 \triangleq \frac{1 - \bar{\alpha}_t - 1}{1 - \bar{\alpha}_t} \beta_t$ to write $x_{t-1} = \frac{1}{\sqrt{\bar{\alpha}_t}}[x_t + \beta_t \nabla_x \ln p_t(x_t)] + \sigma_t z_t$ for $z_t \sim \mathcal{N}(0, I)$.

To exploit side information about x_0 , such as the measurements y in an inverse problem, one can simply replace $p_t(\cdot)$ with $p_t(\cdot|y)$ in the above equations [42]. In the unsupervised case, $s_\theta(x_t, t) \approx \nabla_x \ln p_t(x_t)$ is learned during training but y is presented only during the inference stage, which complicates the evaluation of $\nabla_x \ln p_t(x_t|y)$.

There are two major approaches to approximate $\nabla_x \ln p_t(x_t|y)$. The first uses the Bayes rule to write $\nabla_x \ln p_t(x_t|y) = \nabla_x \ln p_t(x_t) + \nabla_x \ln p_t(y|x_t)$ and then replaces $\nabla_x \ln p_t(x_t)$ with the score approximation $s_\theta(x_t, t)$. But $\nabla_x \ln p_t(y|x_t)$ is intractable because $p_t(y|x_t) = \int p(y|x_0)p(x_0|x_t) dx_0$ with unknown $p(x_0|x_t)$, and so several approximations have been proposed. For example, DPS [7] approximates $p(x_0|x_t)$ as $\delta(x_0 - \hat{x}_{0|t})$, where $\hat{x}_{0|t}$ is the approximation of $E\{x_0|x_t\}$ computed from $s_\theta(x_t, t)$ using Tweedie’s formula [15]:

$$\hat{x}_{0|t} = \frac{x_t + (1 - \bar{\alpha}_t)s_\theta(x_t, t)}{\sqrt{\bar{\alpha}_t}}. \quad (3)$$

Similarly, Π GDM [40] approximates $p(\mathbf{x}_0|\mathbf{x}_t)$ as $\mathcal{N}(\mathbf{x}_0; \hat{\mathbf{x}}_{0|t}, \sigma_{0|t}^2 \mathbf{I})$ for some $\sigma_{0|t}^2$. However, a drawback of these approaches is that they require backpropagation through \mathbf{s}_θ , which i) increases the cost of generating a single sample and ii) prevents efficient batch generation. In Figure 6, we show that DDfire offers a $5\times$ speedup over DPS at an equal number of NFEs.

The second major approach to approximating $\nabla_{\mathbf{x}} \ln p_t(\mathbf{x}_t|\mathbf{y})$ uses Tweedie’s formula and (2) to write

$$\nabla_{\mathbf{x}} \ln p_t(\mathbf{x}_t|\mathbf{y}) = \frac{\sqrt{\bar{\alpha}_t} \mathbb{E}\{\mathbf{x}_0|\mathbf{x}_t, \mathbf{y}\} - \mathbf{x}_t}{1 - \bar{\alpha}_t} \quad (4)$$

and then approximates $\mathbb{E}\{\mathbf{x}_0|\mathbf{x}_t, \mathbf{y}\}$ by a quantity that we’ll refer to as $\hat{\mathbf{x}}_{0|t, \mathbf{y}}$. Note that $\mathbb{E}\{\mathbf{x}_0|\mathbf{x}_t, \mathbf{y}\}$ is the MMSE estimate of \mathbf{x}_0 from the measurements \mathbf{y} and the DDPM information \mathbf{x}_t from (2). For example, assuming \mathbf{y} from (5), DDNM [43] approximates $\mathbb{E}\{\mathbf{x}_0|\mathbf{x}_t, \mathbf{y}\}$ by first computing $\hat{\mathbf{x}}_{0|t}$ and then performing the hard data-consistency step $\hat{\mathbf{x}}_{0|t, \mathbf{y}} = \mathbf{A}^+ \mathbf{y} + (\mathbf{I} - \mathbf{A}^+ \mathbf{A}) \hat{\mathbf{x}}_{0|t}$, where $(\cdot)^+$ denotes pseudo-inverse. DDS [9] and DiffPIR [45] instead use the soft data-consistency step $\hat{\mathbf{x}}_{0|t, \mathbf{y}} = \arg \min_{\mathbf{x}} \|\mathbf{y} - \mathbf{A}\mathbf{x}\|^2 + \rho_t \|\mathbf{x} - \hat{\mathbf{x}}_{0|t}\|^2$ with some $\rho_t > 0$. DDRM [24] is a related technique that requires a singular value decomposition (SVD), which is prohibitive in many applications.

Other ways to solve inverse problems with diffusion are described in the excellent recent overview [10].

3. Approach

We aim to compute an accurate approximation to $\mathbb{E}\{\mathbf{x}_0|\mathbf{x}_t, \mathbf{y}\}$ at each DDPM reverse step t . Unlike existing approaches, we denoise (using the score function \mathbf{s}_θ) multiple times per t and inject colored noise to keep the denoiser input-error white (i.e., “on the manifold” [6]). To constrain the total number of neural function evaluations (NFEs), we subsample DDPM’s $\{t\}$ sequence using DDIM [39].

We consider two classes of inverse problem: i) the standard linear model (SLM), where

$$\mathbf{y} = \mathbf{A}\mathbf{x}_0 + \mathbf{w}/\sqrt{\gamma_w}, \quad \mathbf{w} \sim \mathcal{N}(\mathbf{0}, \mathbf{I}_m), \quad (5)$$

for noise precision (i.e., inverse variance) γ_w , and ii) the generalized linear model (GLM), which can handle linear inverse problems with additive non-Gaussian noise, as well as nonlinear inverse problems like phase retrieval [13, 36], Poisson regression [17], and dequantization [47]. The GLM version will be described in Section 3.4.

3.1. Fast iterative renoising (FIRE) for the SLM

A high-level summary of the proposed approach is now given. At each given DDPM step t , we initialize $\mathbf{r} = \mathbf{x}_t/\sqrt{\bar{\alpha}_t}$ (recall (2)), initialize γ at the precision of the error in \mathbf{r} , which equals

$$\gamma_t \triangleq \frac{\bar{\alpha}_t}{1 - \bar{\alpha}_t}, \quad (6)$$

and then repeat the following steps I_t times:

1. Denoise \mathbf{r} to yield $\bar{\mathbf{x}}_0$ and estimate its error precision η .
2. Linearly estimate \mathbf{x}_0 using the measurements \mathbf{y} and the denoiser output $\bar{\mathbf{x}}_0$, yielding $\hat{\mathbf{x}}_0$.
3. Renoise: Increase the target error precision γ by factor ρ and, with appropriate noise \mathbf{n} , set $\mathbf{r} = \hat{\mathbf{x}}_0 + \mathbf{n}$ so that $\mathbf{r} \sim \mathcal{N}(\mathbf{x}_0, \mathbf{I}/\gamma)$.

The quantity $\hat{\mathbf{x}}_0$ is used to approximate $\mathbb{E}\{\mathbf{x}_0|\mathbf{x}_t, \mathbf{y}\}$ in (4). Details are given below.

From Tweedie’s formula (3), we can write the denoiser of any $\tilde{\mathbf{x}} = \mathbf{x}_0 + \epsilon/\sqrt{\gamma}$ with $\epsilon \sim \mathcal{N}(\mathbf{0}, \mathbf{I})$ as

$$\mathbf{d}(\tilde{\mathbf{x}}, \gamma) \triangleq \frac{\tilde{\mathbf{x}} + (1 - \bar{\alpha}_t) \mathbf{s}_\theta(\tilde{\mathbf{x}}, t)}{\sqrt{\bar{\alpha}_t}} \Big|_{t=\hat{t}(\gamma)}, \quad (7)$$

where $\hat{t}(\gamma) \triangleq \arg \min_{t=1,2,\dots,T} |\gamma_t - \gamma|$ is the DDPM step t whose precision γ_t from (6) is closest to γ .

For FIRE, we need a statistical model for the denoiser output error. It would be convenient if we could model the denoiser output error as AWGN, but this is not true for $\mathbf{d}(\tilde{\mathbf{x}}, \gamma)$. To help promote an AWGN error model, we add AWGN to $\mathbf{d}(\tilde{\mathbf{x}}, \gamma)$ with variance that matches the pixelwise average error variance in $\mathbf{d}(\tilde{\mathbf{x}}, \gamma)$. The corresponding precision can be precomputed for each DDPM step t as follows

$$\eta_t \triangleq \mathbb{E}\{\|\mathbf{d}(\mathbf{x}_0 + \epsilon/\sqrt{\gamma_t}, \gamma_t) - \mathbf{x}_0\|^2/d\}^{-1}, \quad (8)$$

where the expectation is over $\epsilon \sim \mathcal{N}(\mathbf{0}, \mathbf{I})$ and validation images $\mathbf{x}_0 \sim p_0$, and d is the dimension of \mathbf{x}_0 . The modified denoising step then reads as

$$\bar{\mathbf{x}}_0 = \mathbf{d}(\tilde{\mathbf{x}}, \gamma) + \mathbf{v}/\sqrt{\eta_{\hat{t}(\gamma)}}, \quad \mathbf{v} \sim \mathcal{N}(\mathbf{0}, \mathbf{I}). \quad (9)$$

Note that the amount of noise added in (9) grows very small as $t \rightarrow 0$. In the sequel, we assume that

$$\bar{\mathbf{x}}_0 = \mathbf{x}_0 + \mathbf{e}/\sqrt{\eta}, \quad \mathbf{e} \sim \mathcal{N}(\mathbf{0}, \mathbf{I}). \quad (10)$$

To estimate η in (10), we use (5) to write $\mathbb{E}\{\|\mathbf{y} - \mathbf{A}\bar{\mathbf{x}}_0\|^2\} = m/\gamma_w + \|\mathbf{A}\|_F^2/\eta$, which suggests setting η using

$$\eta \approx \|\mathbf{A}\|_F^2 (\|\mathbf{y} - \mathbf{A}\bar{\mathbf{x}}_0\|^2 - m/\gamma_w)^{-1}. \quad (11)$$

Figure S2 shows that η accurately tracks $d/\|\mathbf{x}_0 - \bar{\mathbf{x}}_0\|^2$. Without an SVD, we can use $\|\mathbf{A}\|_F^2 \approx \frac{1}{L} \sum_{l=1}^L \|\mathbf{A}\mathbf{w}_l\|^2$ with i.i.d. $\mathbf{w}_l \sim \mathcal{N}(\mathbf{0}, \mathbf{I})$ and large enough L .

To linearly estimate \mathbf{x}_0 from the measurements \mathbf{y} and the denoiser output $\bar{\mathbf{x}}_0$, we compute, for some $\hat{\gamma}_w$,

$$\hat{\mathbf{x}}_0 \triangleq \arg \min_{\mathbf{x}} \{\hat{\gamma}_w \|\mathbf{y} - \mathbf{A}\mathbf{x}\|^2 + \eta \|\mathbf{x} - \bar{\mathbf{x}}_0\|^2\} \quad (12)$$

using conjugate gradients (CG). For any $\eta > 0$, this gives

$$\hat{\mathbf{x}}_0 = (\bar{\mathbf{A}}^H \bar{\mathbf{A}})^{-1} \bar{\mathbf{A}}^H \bar{\mathbf{y}}, \quad \bar{\mathbf{y}} \triangleq \begin{bmatrix} \sqrt{\hat{\gamma}_w} \mathbf{y} \\ \sqrt{\eta} \bar{\mathbf{x}}_0 \end{bmatrix}, \quad \bar{\mathbf{A}} \triangleq \begin{bmatrix} \sqrt{\hat{\gamma}_w} \mathbf{A} \\ \sqrt{\eta} \mathbf{I} \end{bmatrix}. \quad (13)$$

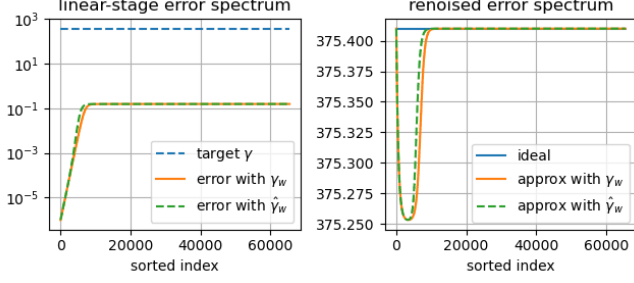


Figure 2. For FFHQ Gaussian deblurring with both $\hat{\gamma}_w$ from (17) and $\hat{\gamma}_w = \gamma_w$, the left shows the error spectrum $\text{diag}(\mathbf{V}^H \mathbf{C} \mathbf{V})$ of the linear estimate $\hat{\mathbf{x}}_0$ and the right shows the ideal renoised spectrum $\mathbf{1}/\gamma$ and its FIRE approximation $\text{diag}(\mathbf{V}^H \mathbf{C} \mathbf{V}) + \hat{\boldsymbol{\lambda}}$. Here we used $\gamma_w = 10^6$, DDPM step $t = 1000$, and $\rho = 66$.

When $\hat{\gamma}_w = \gamma_w$, (5) and (10) imply that $\hat{\mathbf{x}}_0$ is the minimum variance unbiased estimate (MVUE) of \mathbf{x}_0 . For general $\hat{\gamma}_w$,

$$\hat{\mathbf{x}}_0 = (\hat{\gamma}_w \mathbf{A}^H \mathbf{A} + \eta \mathbf{I})^{-1} (\hat{\gamma}_w \mathbf{A}^H \mathbf{y} + \eta \bar{\mathbf{x}}_0) \quad (14)$$

$$= \mathbf{x}_0 + (\hat{\gamma}_w \mathbf{A}^H \mathbf{A} + \eta \mathbf{I})^{-1} (\frac{\hat{\gamma}_w}{\sqrt{\hat{\gamma}_w}} \mathbf{A}^H \mathbf{w} + \sqrt{\eta} \mathbf{e}), \quad (15)$$

and so $\hat{\mathbf{x}}_0 \sim \mathcal{N}(\mathbf{x}_0, \mathbf{C})$ with covariance

$$\mathbf{C} \triangleq (\bar{\mathbf{A}}^H \bar{\mathbf{A}})^{-1} (\frac{\hat{\gamma}_w^2}{\gamma_w} \mathbf{A}^H \mathbf{A} + \eta \mathbf{I}) (\bar{\mathbf{A}}^H \bar{\mathbf{A}})^{-1}. \quad (16)$$

By setting $\hat{\gamma}_w < \gamma_w$, we can reduce the condition number $\text{cond}(\bar{\mathbf{A}}^H \bar{\mathbf{A}})$ and thus speed up CG [26]. In the typical case that $\|\mathbf{A}\|_2 = 1$, we have that $\text{cond}(\bar{\mathbf{A}}^H \bar{\mathbf{A}}) \leq \hat{\gamma}_w/\eta$, and so we can guarantee $\text{cond}(\bar{\mathbf{A}}^H \bar{\mathbf{A}}) \leq 10^4$ by setting

$$\hat{\gamma}_w = \eta \min\{10^4, \gamma_w/\eta\}. \quad (17)$$

Although setting $\hat{\gamma}_w < \gamma_w$ will degrade $\hat{\mathbf{x}}_0$ relative to the MVUE (see Fig. 2), the degradation is offset by the fact that less noise will be added in the renoising stage below.

For renoising, we generate $\mathbf{n} \sim \mathcal{N}(\mathbf{0}, \boldsymbol{\Sigma})$ so that the error in the renoised estimate $\mathbf{r} \triangleq \hat{\mathbf{x}}_0 + \mathbf{n}$ is AWGN with target precision γ . From (5), (10), (15), and (16), we need

$$\boldsymbol{\Sigma} = \frac{1}{\gamma} \mathbf{I} - \mathbf{C}, \quad (18)$$

where γ must be small enough that $\boldsymbol{\Sigma} \geq 0$. In terms of the SVD $\mathbf{A} = \mathbf{U} \mathbf{S} \mathbf{V}^H$ with $s_n \triangleq [\mathbf{S}]_{n,n}$, we know that

$$\boldsymbol{\Sigma} = \mathbf{V} \text{Diag}(\boldsymbol{\lambda}) \mathbf{V}^H \text{ for } \lambda_n = \frac{1}{\gamma} - \frac{s_n^2 \hat{\gamma}_w^2 / \gamma_w + \eta}{[s_n^2 \hat{\gamma}_w + \eta]^2}. \quad (19)$$

If that SVD was available, we could generate $\mathbf{n} \sim \mathcal{N}(\mathbf{0}, \boldsymbol{\Sigma})$ using $\mathbf{n} = \mathbf{V} \text{Diag}(\boldsymbol{\lambda})^{\frac{1}{2}} \boldsymbol{\varepsilon}$ for $\boldsymbol{\varepsilon} \sim \mathcal{N}(\mathbf{0}, \mathbf{I})$. But when an SVD is unavailable, we approximate $\boldsymbol{\Sigma}$ in (18) by

$$\hat{\boldsymbol{\Sigma}} = (\frac{1}{\gamma} - \frac{1}{\eta}) \mathbf{I} + \xi \mathbf{A}^H \mathbf{A} \quad (20)$$

$$= \mathbf{V} \text{Diag}(\hat{\boldsymbol{\lambda}}) \mathbf{V}^H \text{ for } \hat{\lambda}_n = \frac{1}{\gamma} - \frac{1}{\eta} + \xi s_n^2 \quad (21)$$

for $\gamma \leq \eta$ and some $\xi \geq 0$. Notice that the approximation is perfect (i.e., $\hat{\lambda}_n = \lambda_n$) for all n such that $s_n = 0$. Setting¹

$$\xi = \frac{1}{s_{\max}^2} \left(\frac{1}{\eta} - \frac{s_{\max}^2 \hat{\gamma}_w^2 / \gamma_w + \eta}{[s_{\max}^2 \hat{\gamma}_w + \eta]^2} \right), \quad (22)$$

we also get a perfect noise approximation at all n for which $s_n = \max_n s_n \triangleq s_{\max}$. If s_{\max} was unknown, it could be easily computed using the power iteration [33]. Finally, to generate $\mathbf{n} \sim \mathcal{N}(\mathbf{0}, \hat{\boldsymbol{\Sigma}})$, we use

$$\mathbf{n} = \left[\sqrt{\frac{1}{\gamma} - \frac{1}{\eta}} \mathbf{I}_d \sqrt{\xi} \mathbf{A}^H \right] \boldsymbol{\varepsilon}, \quad \boldsymbol{\varepsilon} \sim \mathcal{N}(\mathbf{0}, \mathbf{I}_{d+m}) \quad (23)$$

and then renoise via $\mathbf{r} = \hat{\mathbf{x}}_0 + \mathbf{n}$. Figure 2 shows the agreement between the ideal and approximate renoised spectra.

3.2. DDIM sampling

To control the total NFES, we use DDIM [39] to subsample DDPM's steps $\{1, \dots, T\}$ down to $\{t[k]\}_{k=1}^K$ for some K . DDIM's forward process yields, for $k = 1, \dots, K$,

$$\mathbf{x}_k = \sqrt{\bar{\alpha}_{t[k]}} \mathbf{x}_0 + \sqrt{1 - \bar{\alpha}_{t[k]}} \boldsymbol{\varepsilon}_k, \quad \boldsymbol{\varepsilon}_k \sim \mathcal{N}(\mathbf{0}, \mathbf{I}) \quad (24)$$

where we've slightly abused our earlier notation in that DDIM's \mathbf{x}_k is equivalent to DDPM's $\mathbf{x}_{t[k]}$. The DDIM reverse process can be written (see Sec. S1)

$$\mathbf{x}_{k-1} = c_k \mathbf{x}_k + g_k \mathbb{E}\{\mathbf{x}_0 | \mathbf{x}_k, \mathbf{y}\} + \sigma_k \mathbf{w}_k \quad (25)$$

$$\sigma_k = \eta_{\text{ddim}} \sqrt{\frac{1 - \bar{\alpha}_{t[k-1]}}{1 - \bar{\alpha}_{t[k]}}} \sqrt{1 - \frac{\bar{\alpha}_{t[k]}}{\bar{\alpha}_{t[k-1]}}} \quad (26)$$

$$c_k = \sqrt{\frac{1 - \bar{\alpha}_{t[k-1]} - \sigma_k^2}{1 - \bar{\alpha}_{t[k]}}, \quad g_k = \sqrt{\bar{\alpha}_{t[k-1]}} - c_k \sqrt{\bar{\alpha}_{t[k]}} \quad (27)$$

for $\mathbf{w}_k \sim \mathcal{N}(\mathbf{0}, \mathbf{I}) \forall k$ and initialization $\mathbf{x}_K \sim \mathcal{N}(\mathbf{0}, \mathbf{I})$. Algorithm 1 details DDIM with the FIRE approximation of $\mathbb{E}\{\mathbf{x}_0 | \mathbf{x}_k, \mathbf{y}\}$, which we refer to as ‘‘DDfire.’’

3.3. DDfire scheduling

We now discuss how to select the DDIM schedule $\{t[k]\}_{k=1}^K$, the FIRE iteration schedule $\{I_k\}_{k=1}^K$, and the renoising precision-increase-factor ρ to meet a fixed budget of $I_{\text{tot}} \triangleq \sum_{k=1}^K I_k$ NFES.

We treat the number of DDIM steps K as a tuning parameter. To set the DDIM schedule $\{t[k]\}_{k=1}^K$, we match the endpoints to DDPM (i.e., $t[1] = T$ and $t[K] = 1$) and choose the middle $t[k]$ to uniformly partition the DDPM log-precisions $\ln \gamma_t$ (recall (6)). That is, for $k = 1, \dots, K$:

$$t[k] = \arg \min_{t=1, \dots, T} \left| \log \gamma_T + (k-1) \frac{\log \gamma_1 - \log \gamma_T}{K-1} - \log \gamma_t \right|.$$

This way, the dB gain between $\gamma_{t[k]}$ to $\gamma_{t[k+1]}$ is approximately constant over k . See the dashed lines in Fig. 3.

¹It is straightforward to show that $\xi \geq 0$ whenever $\hat{\gamma}_w \leq \gamma_w$.

Algorithm 1 DDfire for the SLM

Require: $\mathbf{y}, \mathbf{A}, \gamma_w, \{I_k\}_{k=1}^K, \rho$

- 1: $\mathbf{x}_K \sim \mathcal{N}(\mathbf{0}, \mathbf{I})$
- 2: **for** $k = K, K-1, \dots, 1$ **do**
- 3: // SLM-FIRE
- 4: $\mathbf{r} \leftarrow \mathbf{x}_k / \sqrt{\alpha_{t[k]}}$, $\gamma \leftarrow \gamma_{t[k]}$ // Initialize
- 5: **for** $i = 1, \dots, I_k$ **do**
- 6: // Denoise
- 7: $\bar{\mathbf{x}}_0 \leftarrow \mathbf{d}(\mathbf{r}, \gamma) + \mathbf{v} / \sqrt{\eta \bar{\gamma}}$, $\mathbf{v} \sim \mathcal{N}(\mathbf{0}, \mathbf{I})$
- 8: $\eta \leftarrow \|\mathbf{A}\|_F^2 (\|\mathbf{y} - \mathbf{A}\bar{\mathbf{x}}_0\|^2 - m/\gamma_w)^{-1}$
- 9: // Linear estimation
- 10: $\hat{\gamma}_w \leftarrow \eta \min\{10^4, \gamma_w/\eta\}$
- 11: $\hat{\mathbf{x}}_0 \leftarrow \arg \min_{\mathbf{x}} \hat{\gamma}_w \|\mathbf{y} - \mathbf{A}\mathbf{x}\|^2 + \eta \|\mathbf{x} - \bar{\mathbf{x}}_0\|^2$
- 12: // Renoise
- 13: $\gamma \leftarrow \min\{\rho\gamma, \eta\}$
- 14: $\xi \leftarrow \frac{1}{s_{\max}^2} \left(\frac{1}{\eta} - \frac{s_{\max}^2 \hat{\gamma}_w^2 / \gamma_w + \eta}{[s_{\max}^2 \hat{\gamma}_w + \eta]^2} \right)$
- 15: $\mathbf{n} \leftarrow \left[\sqrt{\frac{1}{\gamma} - \frac{1}{\eta}} \mathbf{I} \sqrt{\xi} \mathbf{A}^H \right] \boldsymbol{\varepsilon}$, $\boldsymbol{\varepsilon} \sim \mathcal{N}(\mathbf{0}, \mathbf{I})$
- 16: $\mathbf{r} \leftarrow \hat{\mathbf{x}}_0 + \mathbf{n}$
- 17: // DDIM update
- 18: $\mathbf{x}_{k-1} = c_k \mathbf{x}_k + g_k \hat{\mathbf{x}}_0 + \sigma_k \mathbf{w}_k$, $\mathbf{w}_k \sim \mathcal{N}(\mathbf{0}, \mathbf{I})$
- 19: **return** $\hat{\mathbf{x}}_0$

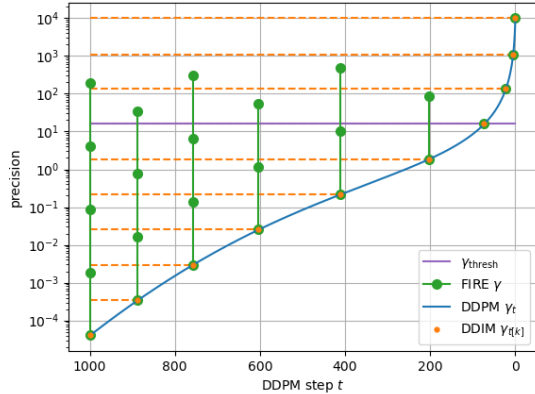


Figure 3. For an FFHQ denoiser: the DDPM precision γ_t versus step t , the DDIM-subsampled $t[k]$ giving log-uniform $\gamma_{t[k]}$, the precision γ_{thresh} corresponding to a $\delta_1 = 0.4$ fraction of single-FIRE-iteration DDIM steps, and the denoiser input precision γ at each FIRE iteration of each DDIM step, for $K = 10$ and $I_{\text{tot}} = 25$.

We set $\{I_k\}_{k=1}^K$ and ρ so that the denoiser output precision η at the final FIRE iteration equals or exceeds a threshold η_{thresh} at all DDIM steps k . Equivalently, the denoiser *input* precision at the final FIRE iteration must equal or exceed some γ_{thresh} at all k . To select γ_{thresh} , we treat the fraction $\delta_1 \in [0, 1)$ of 1-FIRE-iteration DDIM steps as a tuning parameter. For a given δ_1 , we set the number of 1-iteration steps at $K_1 \triangleq 1 + \lfloor (K-1)\delta_1 \rfloor \in \{1, \dots, K-1\}$. We then set the denoiser-input-precision-threshold at the precision of the first 1-iteration DDIM step, i.e., $\gamma_{\text{thresh}} = \gamma_{t[K+1-K_1]}$. We thus need to find a FIRE schedule $\{I_k\}_{k=1}^K$

such that $\gamma_{t[k]}\rho^{I_k-1} \geq \gamma_{\text{thresh}} \forall k$ with positive integer I_k . For a given ρ , it suffices that

$$I_k = \left\lceil \max \left\{ \frac{\log \gamma_{\text{thresh}} - \log \gamma_{t[k]}}{\log \rho}, 0 \right\} + 1 \right\rceil. \quad (28)$$

To find the smallest ρ that meets the NFE budget $I_{\text{tot}} = \sum_{k=1}^K I_k$, with I_k from (28), we use bisection search.

In summary, for NFE budget I_{tot} , we treat the number of DDIM steps $K \in \{1, \dots, I_{\text{tot}}\}$ and the fraction of single-FIRE-iteration steps $\delta_1 \in [0, 1)$ as tuning parameters and, from them, compute $\{t[k]\}_{k=1}^K$, ρ , and $\{I_k\}_{k=1}^K$. See Fig. 3 for an example. Roughly speaking, $K = I_{\text{tot}}/2$ and $\delta_1 = 0.5$ work well, but (K, δ_1) are best tuned via grid search.

3.4. DDfire for the GLM

We now propose to extend the SLM-FIRE from Section 3.1 to the generalized linear model (GLM)

$$\mathbf{y} \sim p(\mathbf{y}|\mathbf{z}_0) = \prod_{j=1}^m p_{y|z}(y_j|z_{0,j}) \quad \text{with } \mathbf{z}_0 \triangleq \mathbf{A}\mathbf{x}_0 \quad (29)$$

where $p_{y|z}$ is some scalar ‘‘measurement channel.’’ Examples include $p_{y|z}(y|z) = \mathcal{N}(y; |z|, 1/\gamma_w)$ for phase retrieval, $p_{y|z}(y|z) = z^y e^{-z}/y!$ for Poisson regression, and $p_{y|z}(y|z) = \int_{\tau_y} \mathcal{N}(\tau; z, 1/\gamma_w) d\tau$ for dequantization.

Our extension is inspired by expectation propagation (EP) [3, 31] and its application to GLMs in [28, 35]. The idea is to iterate between i) constructing pseudo-measurements $\bar{\mathbf{y}} = \mathbf{A}\mathbf{x}_0 + \bar{\mathbf{w}}$ with $\bar{\mathbf{w}} \sim \mathcal{N}(\mathbf{0}, \mathbf{I}/\bar{\gamma}_w)$ using $p_{y|z}$ and an SLM-FIRE-constructed belief that $\mathbf{z}_0 \sim \mathcal{N}(\bar{\mathbf{z}}_0, \mathbf{I}/\bar{\eta}_z)$, and then ii) running SLM-FIRE with those pseudo-measurements and updating its belief on \mathbf{z}_0 . Figure 4 shows a high-level summary. Details are given below.

To construct the belief on \mathbf{z}_0 , we use the SLM-FIRE denoiser output model $\mathbf{x}_0 \sim \mathcal{N}(\bar{\mathbf{x}}_0, \mathbf{I}/\eta)$ from (10). Because $\mathbf{z}_0 = \mathbf{A}\mathbf{x}_0$, we see that $\mathbf{z}_0 \sim \mathcal{N}(\bar{\mathbf{z}}_0, \mathbf{A}\mathbf{A}^H/\eta)$, where $\bar{\mathbf{z}}_0 \triangleq \mathbf{A}\bar{\mathbf{x}}_0$. For simplicity, however, we use the white-noise approximation $\mathbf{z}_0 \sim \mathcal{N}(\bar{\mathbf{z}}_0, \mathbf{I}/\bar{\eta}_z)$, where $\bar{\eta}_z \triangleq \eta m / \|\mathbf{A}\|_F^2$. Using the scalar belief $z_{0,j} \sim \mathcal{N}(\bar{z}_{0,j}, 1/\bar{\eta}_z)$ and the likelihood model $p_{y|z}(y_j|z_{0,j})$, EP suggests to first compute the posterior mean $\mathbb{E}\{z_{0,j}|y_j; \bar{z}_{0,j}, \bar{\eta}_z\} \triangleq \hat{z}_{0,j}$ and variance $\frac{1}{m} \sum_{j=1}^m \text{var}\{z_{0,j}|y_j; \bar{z}_{0,j}, \bar{\eta}_z\} \triangleq 1/\hat{\eta}_z^{-1}$, and then the pass ‘‘extrinsic’’ versions of those quantities back to SLM-FIRE:

$$\bar{\gamma}_w \triangleq \hat{\eta}_z - \bar{\eta}_z, \quad \bar{\mathbf{y}} \triangleq (\hat{\eta}_z \hat{\mathbf{z}}_0 - \bar{\eta}_z \bar{\mathbf{z}}_0) / \bar{\gamma}_w \quad (30)$$

where they parameterize the pseudo-measurement model

$$\bar{\mathbf{y}} = \mathbf{A}\mathbf{x}_0 + \bar{\mathbf{w}} / \sqrt{\bar{\gamma}_w}, \quad \bar{\mathbf{w}} \sim \mathcal{N}(\mathbf{0}, \mathbf{I}). \quad (31)$$

In Fig. S3, we show that GLM-FIRE’s $\bar{\gamma}_w$ accurately tracks the noise precision of $\bar{\mathbf{y}}$.

When $p_{y|z}(y|z) = \mathcal{N}(y; z, 1/\gamma_w)$, is it straightforward to show that $\bar{\mathbf{y}} = \mathbf{y}$ and $\bar{\gamma}_w = \gamma_w$ for any $\bar{\mathbf{z}}_0$ and $\bar{\eta}_z$, in which case GLM-FIRE reverts to SLM-FIRE.

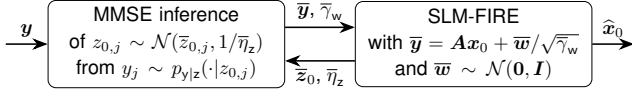


Figure 4. High-level overview of GLM-FIRE, which uses EP-style iterations between SLM-FIRE and an MMSE inference stage that involves the measurement channel $p_{y|z}$.

Algorithm 2 DDfire for the GLM

Require: $\mathbf{y}, \mathbf{A}, \gamma_w, \{I_k\}_{k=1}^K, \rho$

- 1: $\mathbf{x}_K \sim \mathcal{N}(\mathbf{0}, \mathbf{I})$
- 2: **for** $k = K, K-1, \dots, 1$ **do**
- 3: // GLM-FIRE
- 4: $\mathbf{r} \leftarrow \mathbf{x}_k / \sqrt{\alpha_t[k]}, \gamma \leftarrow \gamma_t[k]$ // Initialize
- 5: **for** $i = 1, \dots, I_k$ **do**
- 6: // Denoise
- 7: $\bar{\mathbf{x}}_0 \leftarrow \mathbf{d}(\mathbf{r}, \gamma) + \mathbf{v} / \sqrt{\eta_{\hat{t}}(\gamma)}, \mathbf{v} \sim \mathcal{N}(\mathbf{0}, \mathbf{I})$
- 8: $\eta \leftarrow \eta_{\hat{t}}(\gamma) / 2$
- 9: // Compute pseudo-measurements
- 10: $\bar{\eta}_z \leftarrow \eta m / \|\mathbf{A}\|_F^2$
- 11: $\bar{\mathbf{z}}_0 \leftarrow \mathbf{A} \bar{\mathbf{x}}_0$
- 12: $\hat{\eta}_z \leftarrow m / \sum_{j=1}^m \text{var}\{z_{0,j} | y_j; \bar{\mathbf{z}}_0, \bar{\eta}_z\}$
- 13: $\hat{z}_{0,j} \leftarrow \mathbb{E}\{z_{0,j} | y_j; \bar{\mathbf{z}}_0, \bar{\eta}_z\} \forall j$
- 14: $\hat{\gamma}_w \leftarrow \hat{\eta}_z - \bar{\eta}_z$
- 15: $\bar{\mathbf{y}} \leftarrow (\hat{\eta}_z \hat{\mathbf{z}}_0 - \bar{\eta}_z \bar{\mathbf{z}}_0) / \hat{\gamma}_w$
- 16: $\eta \leftarrow \|\mathbf{A}\|_F^2 (\|\bar{\mathbf{y}} - \mathbf{A} \bar{\mathbf{x}}_0\|^2 - m / \hat{\gamma}_w)^{-1}$
- 17: // Linear estimation
- 18: $\hat{\gamma}_w \leftarrow \eta \min\{10^4, \hat{\gamma}_w / \eta\}$
- 19: $\hat{\mathbf{x}}_0 \leftarrow \arg \min_{\mathbf{x}} \hat{\gamma}_w \|\bar{\mathbf{y}} - \mathbf{A} \mathbf{x}\|^2 + \eta \|\mathbf{x} - \bar{\mathbf{x}}_0\|^2$
- 20: // Renoise
- 21: $\gamma \leftarrow \min\{\rho \gamma, \eta\}$
- 22: $\xi \leftarrow \frac{1}{s_{\max}^2} \left(\frac{1}{\eta} - \frac{s_{\max}^2 \hat{\gamma}_w^2 / \hat{\gamma}_w + \eta}{[s_{\max}^2 \hat{\gamma}_w + \eta]^2} \right)$
- 23: $\mathbf{n} \leftarrow \left[\sqrt{\frac{1}{\gamma} - \frac{1}{\eta}} \mathbf{I} \sqrt{\xi} \mathbf{A}^H \right] \boldsymbol{\varepsilon}, \boldsymbol{\varepsilon} \sim \mathcal{N}(\mathbf{0}, \mathbf{I})$
- 24: $\mathbf{r} \leftarrow \hat{\mathbf{x}}_0 + \mathbf{n}$
- 25: // DDIM update
- 26: $\mathbf{x}_{k-1} = c_k \mathbf{x}_k + g_k \hat{\mathbf{x}}_0 + \sigma_k \mathbf{w}_k, \mathbf{w}_k \sim \mathcal{N}(\mathbf{0}, \mathbf{I})$
- 27: **return** $\hat{\mathbf{x}}_0$

In the GLM version of DDfire, we perform one EP update per FIRE iteration, as detailed in Alg. 2.

3.5. Relation to other diffusion methods

SLM-DDfire would resemble DiffPIR [45] if it used one iteration for every DDIM step (i.e., $I_k = 1 \forall k$), in which case there would be no renoising; both methods first compute $\bar{\mathbf{x}}_0 = \mathbb{E}\{\mathbf{x}_0 | \mathbf{x}_t\}$ and then $\hat{\mathbf{x}}_0 = \arg \min_{\mathbf{x}} \gamma_w \|\mathbf{y} - \mathbf{A} \mathbf{x}\|^2 + \eta \|\mathbf{x} - \bar{\mathbf{x}}_0\|^2$. But DDfire designs η to accurately track the error precision of $\bar{\mathbf{x}}_0$ (see Fig. S2) while DiffPIR sets η at $\lambda \eta_{\hat{t}}(\gamma_t)$ with a tuning parameter λ .

SLM-DDfire’s use of multiple denoising/renoising steps per DDIM iteration k bears some resemblance to RePaint’s use of “time travel” [27]. At step k of RePaint’s reverse process, the DDPM forward process is invoked to trans-

Table 1. DDfire ablation results for noisy FFHQ $4\times$ -super-resolution with $\sqrt{1/\gamma_w} = 0.05$ at 100 NFES.

Method	PSNR \uparrow	LPIPS \downarrow	Runtime
DDfire	27.05	0.2367	6.21s
DDfire w/o including noise in $\bar{\mathbf{x}}_0$	26.73	0.2432	6.21s
DDfire w/o estimating η	24.34	0.2969	6.21s
DDfire w/ $t[k] = \lfloor T - \frac{k-1}{K-1}(T-1) \rfloor$	26.02	0.2617	6.21s
DDfire w/o CG early stopping	27.06	0.2367	32.71s
DDfire w/ SVD	27.06	0.2365	4.97s

form \mathbf{x}_k back to \mathbf{x}_{k+j} for $j \sim 10$ (which involves adding noise), after which j reverse steps are performed to obtain a new \mathbf{x}_k . This time traveling is repeated $r \sim 10$ times at each k , which has the effect of increasing the total NFES by the factor r . While RePaint handles only inpainting problems, DDNM⁺ [43] extends its approach to general AWGN-corrupted linear inverse problems by using an SVD in a manner that closely resembles DDRM [24]. In contrast, SLM-DDfire does not require an SVD and is designed to operate with many fewer NFES.

4. Numerical experiments

We use 256×256 FFHQ [23] and ImageNet [11] datasets with pretrained diffusion models from [7] and [12], respectively. As linear inverse problems, we consider box inpainting with a 128×128 mask, Gaussian deblurring with a 61×61 blur kernel and standard deviation 3 pixels, motion deblurring with a 61×61 blur kernel and intensity 0.5 generated using [4], and $4\times$ bicubic super-resolution. We compare to DDRM [24] and DiffPIR [45] at 20 NFES, IIGDM [40] and DiffPIR at 100 NFES, and DPS [7] at 1000 NFES.

We also consider phase retrieval with the shot-noise corruption mechanism from [30] for both oversampled Fourier (OSF) and coded diffraction pattern (CDP) [5] \mathbf{A} at $4\times$ oversampling with $\alpha_{\text{shot}} = 8$ and 45, respectively. Here, α_{shot} is the shot-noise strength, as detailed in Sec. S2. We compare to prDeep [30], DOLPH [37], DPS, and the classical hybrid input-output (HIO) algorithm [16].

For DDfire, we tuned the (K, δ_1) hyperparameters to minimize LPIPS on a separate 100-sample test set (see the values in Tables S1 and S2) and we did not use an SVD unless otherwise specified. For phase-retrieval, we used $p_{y|z}(y|z) = \mathcal{N}(y; |z|, 1/\gamma_w)$ for all algorithms. Since this makes the conditional mean and variance in lines 12-13 of Alg. 2 intractable, we used the Laplace approximation [3].

Section S2 contains additional details on the implementation of DDfire and the competing methods.

4.1. Ablation study

We first perform an ablation study on the SLM-DDfire design choices in Section 3.1 using noisy FFHQ $4\times$ -super-resolution and 100 NFES. The results are summarized in

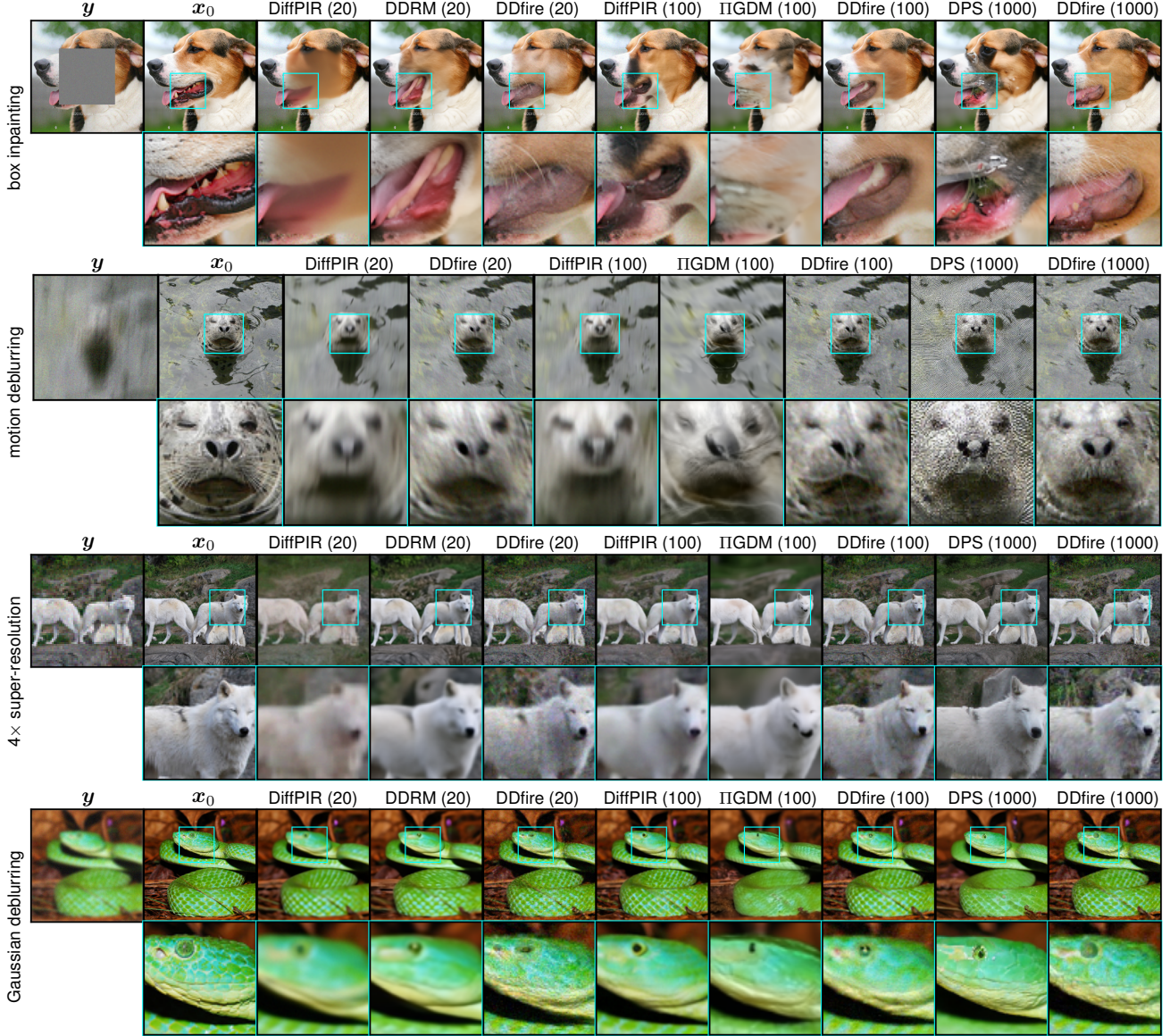


Figure 5. Example recoveries from noisy linear inverse problems with ImageNet images.

Table 1. Not including the AWGN in the denoiser output \bar{x}_0 , as in (9), slightly degrades both the PSNR and LPIPS. A more significant degradation results when η is not estimated via (11) but set at $\eta_{\hat{t}(\gamma)}/2$. Choosing the DDIM schedule $\{t[k]\}_{k=1}^K$ to uniformly sample via $t[k] = \lfloor T - \frac{k-1}{K-1}(T-1) \rfloor$ instead of uniformly partitioning the DDPM log-precisions $\ln \gamma_t$ also degrades PSNR and LPIPS. On the other hand, CG without early stopping gives essentially identical PSNR and LPIPS at the expense of significantly higher runtime. Finally, using an SVD, which obviates both CG and the noise approximation in (21), gives essentially identical PSNR and LPIPS but faster runtime.

4.2. PSNR, LPIPS, and FID results

For noisy linear inverse problems, Tables 2-3 show PSNR, LPIPS [44], and FID [20] on a 1000-sample test set for FFHQ and ImageNet data, respectively. (Noiseless results are reported in Table S3.) We were unable to run DDRM on motion deblurring due to the lack of an SVD. Tables 2-3 show that, when comparing to competitors at equal NFes, DDfire wins in most cases and otherwise performs well.

Fig. 5 shows image examples for inpainting, motion deblurring, Gaussian deblurring, and $4\times$ super-resolution on ImageNet. The zoomed regions show that DDfire does a better job recovering fine details. Additional examples can be found in Fig. S5.

Table 2. Noisy FFHQ results with measurement noise standard deviation $\sqrt{1/\gamma_w} = 0.05$.

# NFEs	Model	Inpaint (box)			Deblur (Gaussian)			Deblur (Motion)			4× Super-resolution		
		PSNR↑	LPIPS↓	FID↓	PSNR↑	LPIPS↓	FID↓	PSNR↑	LPIPS↓	FID↓	PSNR↑	LPIPS↓	FID↓
20	DiffPIR	20.87	0.2741	41.50	23.55	0.3269	41.29	27.31	0.2704	29.27	22.32	0.3560	44.85
	DDRM	22.02	0.2052	40.61	26.27	0.2896	51.70	-	-	-	28.62	0.2417	45.82
	DDfire	21.80	0.1974	28.49	27.18	0.2843	36.22	28.52	0.2455	28.86	27.02	0.2917	37.72
100	DiffPIR	22.44	0.2415	31.98	24.57	0.2936	34.82	26.91	0.2683	26.67	26.76	0.3061	32.33
	IIIGDM	21.75	0.2614	44.41	24.34	0.3125	45.34	25.94	0.2706	41.95	25.42	0.3109	51.41
	DDfire	23.78	0.1623	26.75	27.48	0.2274	25.48	27.79	0.2193	25.91	27.20	0.2399	26.24
1000	DPS	22.84	0.1793	35.69	26.32	0.2327	25.18	27.64	0.2176	27.17	27.11	0.2360	27.38
	DDfire	24.14	0.1579	24.56	26.84	0.2259	24.68	27.71	0.2155	24.57	27.32	0.2356	25.75

Table 3. Noisy ImageNet results with measurement noise standard deviation $\sqrt{1/\gamma_w} = 0.05$.

# NFEs	Model	Inpaint (box)			Deblur (Gaussian)			Deblur (Motion)			4× Super-resolution		
		PSNR↑	LPIPS↓	FID↓	PSNR↑	LPIPS↓	FID↓	PSNR↑	LPIPS↓	FID↓	PSNR↑	LPIPS↓	FID↓
20	DiffPIR	17.68	0.3533	84.62	20.06	0.5295	113.92	24.81	0.3880	55.99	20.78	0.4745	71.67
	DDRM	18.39	0.2837	67.47	23.12	0.4268	68.78	-	-	-	24.98	0.3462	61.31
	DDfire	18.29	0.2834	67.12	22.35	0.4263	56.73	23.54	0.4093	63.53	22.71	0.4119	56.32
100	DiffPIR	18.02	0.3323	65.55	21.31	0.4354	56.35	24.36	0.3685	54.11	23.27	0.4131	63.48
	IIIGDM	17.92	0.3939	86.36	21.54	0.4946	75.43	22.69	0.4391	70.91	22.21	0.4907	78.57
	DDfire	19.56	0.2494	59.70	23.48	0.3712	53.13	23.83	0.3681	53.92	22.94	0.3724	52.35
1000	DPS	18.36	0.2814	59.10	21.67	0.4003	50.46	22.08	0.3905	80.27	23.83	0.3536	49.86
	DDfire	19.68	0.2404	54.96	22.34	0.3552	50.28	24.37	0.3395	51.99	23.22	0.3705	51.19

Table 4. Noisy FFHQ phase retrieval results

# NFEs	Model	OSF			CDP		
		PSNR↑	LPIPS↓	FID↓	PSNR↑	LPIPS↓	FID↓
-	HIO	23.66	0.5299	130.58	17.59	0.5818	84.87
1000	DOLPH	14.73	0.7089	389.88	25.76	0.2163	32.93
1000	DPS	23.63	0.3326	53.91	29.19	0.1994	27.87
800	prDeep	30.90	0.1585	31.51	19.24	0.4352	59.44
800	DDfire	33.56	0.1160	28.94	30.01	0.1767	23.49
100	DDfire	25.88	0.2643	46.54	30.16	0.1707	23.30

Table 4 shows performance on noisy FFHQ phase retrieval. For OSF \mathcal{A} , we see that DDfire at 800 NFEs outperforms prDeep by a small margin and both DPS and DOLPH by a large margin. Also, DDfire at 100 NFEs beats DPS and DOLPH at 1000 NFEs. For CDP \mathcal{A} , we see that DDfire performs similarly at 100 and 800 NFEs and that both outperform the other methods. Example reconstructions for phase retrieval can be found in Fig. S4.

4.3. Runtime results

Figure 6 shows runtime vs. the number of generated samples. DDfire supports batch generation, which increases its efficiency over methods that don't. And when an SVD is available, DDfire can exploit it to reduce runtime. Note the 5× speedup over DPS when both use 1000 NFEs.

5. Conclusion

We proposed DDfire, an unsupervised approach to solving inverse problems using Fast Iterative Renoising (FIRE).

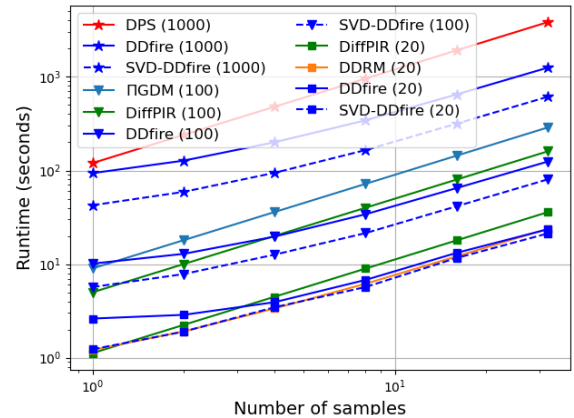


Figure 6. Runtime vs. # of samples for noisy 4× super-resolution on ImageNet. DDfire and DDRM used batch size = # of samples.

FIRE aims to accurately approximate the measurement-conditional score $\nabla_x \ln p_t(x_t|\mathbf{y})$, or equivalently the measurement-conditional denoiser $E\{x_0|x_t, \mathbf{y}\}$, for a fixed budget of NFEs. Experiments on box inpainting, Gaussian and motion deblurring, and 4× super-resolution with FFHQ and ImageNet images show DDfire outperforming DPS, IIIGDM, DiffPIR, and DDRM at equal NFEs on PSNR, LPIPS, and FID in most cases. Experiments on noisy FFHQ phase retrieval (both OSF and CDP versions) show DDfire outperforming DPS, DOLPH, prDeep, and HIO in all cases. In terms of runtime, DDfire supports batch generation and can leverage an SVD for speedup, if available.

References

- [1] Tamir Bendory, Robert Beinert, and Yonina C Eldar. Fourier phase retrieval: Uniqueness and algorithms. In *MATHEON Conf. Compressed Sensing and its Applications*, pages 55–91, 2015. 1
- [2] Raphael Berthier, Andrea Montanari, and Phan-Minh Nguyen. State evolution for approximate message passing with non-separable functions. *Info. Inference*, 9(1):33–79, 2019. 1
- [3] C. M. Bishop. *Pattern Recognition and Machine Learning*. Springer, New York, 2007. 5, 6
- [4] Levi Borodenko. motionblur. Downloaded from <https://github.com/LeviBorodenko/motionblur>, 2020. 6, 1
- [5] E. J. Candès, X. Li, and M. Soltanolkotabi. Phase retrieval from coded diffraction patterns. *Appl. Comput. Harmonic Anal.*, 39(2):277–299, 2015. 6
- [6] Hyungjin Chung, Byeongsu Sim, Dohoon Ryu, and Jong Chul Ye. Improving diffusion models for inverse problems using manifold constraints. In *Proc. Neural Info. Process. Syst. Conf.*, pages 25683–25696, 2022. 3
- [7] Hyungjin Chung, Jeongsol Kim, Michael T McCann, Marc L Klasky, and Jong Chul Ye. Diffusion posterior sampling for general noisy inverse problems. In *Proc. Intl. Conf. Learn. Rep.*, 2023. 1, 2, 6
- [8] Hyungjin Chung, Jeongsol Kim, Michael T McCann, Marc L Klasky, and Jong Chul Ye. diffusion-posterior-sampling. <https://github.com/DPS2022/diffusion-posterior-sampling>, 2023. 2
- [9] Hyungjin Chung, Suhyeon Lee, and Jong Chul Ye. Decomposed diffusion sampler for accelerating large-scale inverse problems. In *Proc. Intl. Conf. Learn. Rep.*, 2024. 1, 3
- [10] Giannis Daras, Hyungjin Chung, Chieh-Hsin Lai, Yuki Mitsufuji, Jong Chul Ye, Peyman Milanfar, Alexandros G Dimakis, and Mauricio Delbracio. A survey on diffusion models for inverse problems. *arXiv:2410.00083*, 2024. 1, 3
- [11] Jia Deng, Wei Dong, Richard Socher, Li-Jia Li, Kai Li, and Li Fei-Fei. Imagenet: A large-scale hierarchical image database. In *Proc. IEEE Conf. Comp. Vision Pattern Recog.*, pages 248–255, 2009. 6
- [12] P. Dhariwal and A. Nichol. Diffusion models beat GANs on image synthesis. In *Proc. Neural Info. Process. Syst. Conf.*, pages 8780–8794, 2021. 6, 1
- [13] Jonathan Dong, Lorenzo Valzania, Antoine Maillard, Thanh-An Pham, Sylvain Gigan, and Michael Unser. Phase retrieval: From computational imaging to machine learning: A tutorial. *IEEE Signal Process. Mag.*, 40(1):45–57, 2023. 3
- [14] D. L. Donoho, A. Maleki, and A. Montanari. Message passing algorithms for compressed sensing. *Proc. Nat. Acad. Sci.*, 106(45):18914–18919, 2009. 1
- [15] B. Efron. Tweedie’s formula and selection bias. *J. Am. Statist. Assoc.*, 106(496):1602–1614, 2011. 1, 2
- [16] J. R. Fienup. Phase retrieval algorithms: A comparison. *Appl. Optics*, 21(15):2758–2769, 1982. 6
- [17] M. A. T. Figueiredo and J. M Bioucas-Dias. Restoration of Poissonian images using alternating direction optimization. *IEEE Trans. Image Process.*, 19(12):3133–3145, 2010. 3
- [18] A. K. Fletcher, P. Pandit, S. Rangan, S. Sarkar, and P. Schniter. Plug-in estimation in high-dimensional linear inverse problems: A rigorous analysis. In *Proc. Neural Info. Process. Syst. Conf.*, pages 7440–7449, 2018. 1
- [19] Doeke Hekstra, Ian Hunt-Isaak, Jack Greisman, and John Russell. phase-retrieval. <https://github.com/Hekstra-Lab/phase-retrieval>, 2018. 3
- [20] Martin Heusel, Hubert Ramsauer, Thomas Unterthiner, Bernhard Nessler, and Sepp Hochreiter. GANs trained by a two time-scale update rule converge to a local Nash equilibrium. In *Proc. Neural Info. Process. Syst. Conf.*, 2017. 7
- [21] Jonathan Ho, Ajay Jain, and Pieter Abbeel. Denoising diffusion probabilistic models. In *Proc. Neural Info. Process. Syst. Conf.*, pages 6840–6851, 2020. 1, 2
- [22] Aapo Hyvärinen. Estimation of non-normalized statistical models by score matching. *J. Mach. Learn. Res.*, 6:695–709, 2005. 2
- [23] Tero Karras, Samuli Laine, and Timo Aila. A style-based generator architecture for generative adversarial networks. In *Proc. IEEE Conf. Comp. Vision Pattern Recog.*, pages 4396–4405, 2019. 6
- [24] Bahjat Kawar, Michael Elad, Stefano Ermon, and Jiaming Song. Denoising diffusion restoration models. In *Proc. Neural Info. Process. Syst. Conf.*, 2022. 1, 3, 6
- [25] Bahjat Kawar, Michael Elad, Stefano Ermon, and Jiaming Song. Denoising diffusion restoration models. Downloaded from <https://github.com/bahjat-kawar/ddrm>, 2022. 1, 2
- [26] David G Luenberger and Yinyu Ye. *Linear and Nonlinear Programming*. Springer, 2016. 4
- [27] Andreas Lugmayr, Martin Danelljan, Andres Romero, Fisher Yu, Radu Timofte, and Luc Van Gool. Repaint: Inpainting using denoising diffusion probabilistic models. In *Proc. IEEE Conf. Comp. Vision Pattern Recog.*, pages 11461–11471, 2022. 6
- [28] Xiangming Meng, Sheng Wu, and Jiang Zhu. A unified Bayesian inference framework for generalized linear models. *IEEE Signal Process. Lett.*, 25(3):398–402, 2018. 5
- [29] C. A. Metzler. prdeep. <https://github.com/ricedsp/prDeep/tree/master>, 2018. 2
- [30] C. A. Metzler, P. Schniter, A. Veeraraghavan, and R. G. Baraniuk. prDeep: Robust phase retrieval with flexible deep neural networks. In *Proc. Intl. Conf. Mach. Learn.*, pages 3501–3510, 2018. 6, 1, 2, 3
- [31] T. Minka. *A Family of Approximate Algorithms for Bayesian Inference*. PhD thesis, Dept. Comp. Sci. Eng., MIT, Cambridge, MA, USA, 2001. 5
- [32] NVlabs. RED-diff. Downloaded from <https://github.com/NVlabs/RED-diff>, 2023. 2
- [33] Beresford N Parlett. *The symmetric eigenvalue problem*. SIAM, 1998. 4
- [34] S. Rangan, P. Schniter, and A. K. Fletcher. Vector approximate message passing. *IEEE Trans. Info. Theory*, 65(10):6664–6684, 2019. 1

- [35] Philip Schniter, Sundeep Rangan, and Alyson K Fletcher. Vector approximate message passing for the generalized linear model. In *Proc. Asilomar Conf. Signals Syst. Comput.*, pages 1525–1529, 2016. 5
- [36] Yoav Shechtman, Yonina C Eldar, Oren Cohen, Henry Nicholas Chapman, Jianwei Miao, and Mordechai Segev. Phase retrieval with application to optical imaging: A contemporary overview. *IEEE Signal Process. Mag.*, 32(3):87–109, 2015. 3
- [37] Shirin Shoushtari, Jiaming Liu, and Ulugbek S Kamilov. Diffusion models for phase retrieval in computational imaging. In *Proc. Asilomar Conf. Signals Syst. Comput.*, pages 779–783, 2023. 6
- [38] Jascha Sohl-Dickstein, Eric Weiss, Niru Maheswaranathan, and Surya Ganguli. Deep unsupervised learning using nonequilibrium thermodynamics. In *Proc. Intl. Conf. Mach. Learn.*, pages 2256–2265, 2015. 1
- [39] Jiaming Song, Chenlin Meng, and Stefano Ermon. Denoising diffusion implicit models. In *Proc. Intl. Conf. Learn. Rep.*, 2021. 1, 2, 3, 4
- [40] Jiaming Song, Arash Vahdat, Morteza Mardani, and Jan Kautz. Pseudoinverse-guided diffusion models for inverse problems. In *Proc. Intl. Conf. Learn. Rep.*, 2023. 1, 3, 6
- [41] Yang Song and Stefano Ermon. Generative modeling by estimating gradients of the data distribution. In *Proc. Neural Info. Process. Syst. Conf.*, 2019. 1
- [42] Yang Song, Jascha Sohl-Dickstein, Diederik P Kingma, Abhishek Kumar, Stefano Ermon, and Ben Poole. Score-based generative modeling through stochastic differential equations. In *Proc. Intl. Conf. Learn. Rep.*, 2021. 1, 2
- [43] Yinhuai Wang, Jiwen Yu, and Jian Zhang. Zero-shot image restoration using denoising diffusion null-space model. In *Proc. Intl. Conf. Learn. Rep.*, 2023. 1, 3, 6
- [44] Richard Zhang, Phillip Isola, Alexei A Efros, Eli Shechtman, and Oliver Wang. The unreasonable effectiveness of deep features as a perceptual metric. In *Proc. IEEE Conf. Comp. Vision Pattern Recog.*, pages 586–595, 2018. 7
- [45] Yuanzhi Zhu, Kai Zhang, Jingyun Liang, Jiezhong Cao, Bihan Wen, Radu Timofte, and Luc Van Gool. Denoising diffusion models for plug-and-play image restoration. In *Proc. IEEE Conf. Comp. Vision Pattern Recog.*, pages 1219–1229, 2023. 1, 3, 6, 2
- [46] Yuanzhi Zhu, Kai Zhang, Jingyun Liang, Jiezhong Cao, Bihan Wen, Radu Timofte, and Luc Van Gool. Diffpir. Downloaded from <https://github.com/yuanzhi-zhu/DiffPIR>, 2024. 2
- [47] A. Zymnis, S. Boyd, and E Candès. Compressed sensing with quantized measurements. *IEEE Signal Process. Lett.*, 17(2):149–152, 2010. 3

Solving Inverse Problems using Diffusion with Fast Iterative Renoising

Supplementary Material

S1. DDIM details

Adapting the first two equations in [39, App.D.3] to our notation gives

$$\begin{aligned} \mathbf{x}_{k-1} &= \sqrt{\bar{\alpha}_{t[k-1]}} \left(\frac{\mathbf{x}_k - \sqrt{1 - \bar{\alpha}_{t[k]}} \mathbb{E}\{\boldsymbol{\epsilon}_k | \mathbf{x}_k\}}{\sqrt{\bar{\alpha}_{t[k]}}} \right) \\ &\quad + \sqrt{1 - \bar{\alpha}_{t[k-1]} - \sigma_k^2} \mathbb{E}\{\boldsymbol{\epsilon}_k | \mathbf{x}_k\} + \sigma_k \mathbf{n}_k \end{aligned} \quad (32)$$

and

$$\sigma_k = \eta_{\text{ddim}} \sqrt{\frac{1 - \bar{\alpha}_{t[k-1]}}{1 - \bar{\alpha}_{t[k]}}} \sqrt{1 - \frac{\bar{\alpha}_{t[k]}}{\bar{\alpha}_{t[k-1]}}}, \quad (33)$$

where $\mathbf{n}_k \sim \mathcal{N}(\mathbf{0}, \mathbf{I})$. Applying $\mathbb{E}\{\cdot | \mathbf{x}_k\}$ to both sides of (24) gives

$$\mathbf{x}_k = \sqrt{\bar{\alpha}_{t[k]}} \mathbb{E}\{\mathbf{x}_0 | \mathbf{x}_k\} + \sqrt{1 - \bar{\alpha}_{t[k]}} \mathbb{E}\{\boldsymbol{\epsilon}_k | \mathbf{x}_k\}, \quad (34)$$

which implies

$$\mathbb{E}\{\boldsymbol{\epsilon}_k | \mathbf{x}_k\} = \frac{\mathbf{x}_k - \sqrt{\bar{\alpha}_{t[k]}} \mathbb{E}\{\mathbf{x}_0 | \mathbf{x}_k\}}{\sqrt{1 - \bar{\alpha}_{t[k]}}}. \quad (35)$$

Plugging (35) into (32) gives

$$\mathbf{x}_{k-1} = \sqrt{\bar{\alpha}_{t[k-1]}} \mathbb{E}\{\mathbf{x}_0 | \mathbf{x}_k\} + \sigma_k \mathbf{n}_k \quad (36)$$

$$+ \sqrt{1 - \bar{\alpha}_{t[k-1]} - \sigma_k^2} \left(\frac{\mathbf{x}_k - \sqrt{\bar{\alpha}_{t[k]}} \mathbb{E}\{\mathbf{x}_0 | \mathbf{x}_k\}}{\sqrt{1 - \bar{\alpha}_{t[k]}}} \right)$$

$$= \sqrt{\bar{\alpha}_{t[k-1]}} \mathbb{E}\{\mathbf{x}_0 | \mathbf{x}_k\} + \sigma_k \mathbf{n}_k \\ + c_k (\mathbf{x}_k - \sqrt{\bar{\alpha}_{t[k]}} \mathbb{E}\{\mathbf{x}_0 | \mathbf{x}_k\}) \quad (37)$$

$$= c_k \mathbf{x}_k + g_k \mathbb{E}\{\mathbf{x}_0 | \mathbf{x}_k\} + \sigma_k \mathbf{n}_k \quad (38)$$

for

$$c_k \triangleq \sqrt{\frac{1 - \bar{\alpha}_{t[k-1]} - \sigma_k^2}{1 - \bar{\alpha}_{t[k]}}} \quad (39)$$

$$g_k \triangleq \sqrt{\bar{\alpha}_{t[k-1]} - c_k \sqrt{\bar{\alpha}_{t[k]}}}, \quad (40)$$

which gives (25)-(27).

S2. Implementation details

S2.1. Inverse problems

For the linear inverse problems, the measurements were generated as

$$\mathbf{y} = \mathbf{A}\mathbf{x}_0 + \mathbf{w}/\sqrt{\gamma_w}, \quad \mathbf{w} \sim \mathcal{N}(\mathbf{0}, \mathbf{I}) \quad (41)$$

with appropriate \mathbf{A} . For box inpainting, Gaussian deblurring, and super-resolution we used the \mathbf{A} and \mathbf{A}^H implementations from [25]. For motion deblurring, we implemented our own \mathbf{A} and \mathbf{A}^H with reflect padding. All methods used these operators implementations except DiffPIR, which used the authors' implementations. Motion-blur kernels were generated using [4].

For phase retrieval, the measurements were generated using the method from [30]:

$$y_j^2 = |z_{0,j}|^2 + w_j, \quad w_j \sim \mathcal{N}(0, \alpha_{\text{shot}}^2 |z_{0,j}|^2), \quad j = 1, \dots, m, \quad (42)$$

where α_{shot} controls the noise level and $\mathbf{z}_0 = \mathbf{A}\mathbf{x}_0$, with the values of \mathbf{x}_0 scaled to lie in the range $[0, 255]$. This is an approximation of the Poisson shot-noise corruption model in that the intensity $y_j^2/\alpha_{\text{shot}}^2$ is approximately Poisson($(|z_{0,j}|/\alpha_{\text{shot}})^2$) distributed for sufficiently small values of α_{shot} . We implemented the oversampled-Fourier \mathbf{A} by zero-padding the image by $2\times$ in each direction and then passing the result through a unitary FFT. For CDP phase retrieval, we set $\mathbf{A} = [\mathbf{A}_1^T, \dots, \mathbf{A}_L^T]^T$ for $\mathbf{A}_l = L^{-1/2} \mathbf{F} \text{Diag}(c_l)$, where \mathbf{F} is a $d \times d$ FFT and c_l contain i.i.d. random entries uniformly distributed on the unit circle in the complex plane, and where $L = 4$. In both cases, $\mathbf{A}^H \mathbf{A} = \mathbf{I}$.

S2.2. Evaluation protocol

For the linear inverse problems, we run each method once for each measurement \mathbf{y} in the 1000-sample test set and compute average PSNR, average LPIPS, and FID from the resulting recoveries.

For OSF phase retrieval, following [7], we run each algorithm four times and keep the reconstruction $\hat{\mathbf{x}}_0$ that minimizes the measurement residual $\|\mathbf{y} - |\mathbf{A}\hat{\mathbf{x}}_0|\|$. Performance metrics are then evaluated after resolving the inherent spatial shift and conjugate flip ambiguities associated with phase retrieval (see, e.g., [1]). Note global phase ambiguity is not an issue due to the non-negativity of our images. For the CDP experiments, we run each algorithm only once and don't perform ambiguity resolution, because it is unnecessary.

S2.3. Unconditional diffusion models

For the FFHQ experiments, all methods used the pretrained model from [7]. For the ImageNet experiments, all methods used the pretrained model from [12]. In both cases, $T = 1000$.

Table S1. Hyperparameter values used for DDfire.

# NFEs	Dataset	$\sqrt{1/\gamma_w}$	Inpaint (box)		Deblur (Gaussian)		Deblur (Motion)		4× Super-resolution	
			K	δ_1	K	δ_1	K	δ_1	K	δ_1
20	FFHQ	0.00	5	0.25	10	0.25	10	0.25	10	0.25
	FFHQ	0.05	10	0.50	10	0.50	8	0.20	10	0.50
	ImageNet	0.05	10	0.50	15	0.10	8	0.20	15	0.25
100	FFHQ	0.00	20	0.25	50	0.25	50	0.25	50	0.25
	FFHQ	0.05	20	0.50	50	0.50	50	0.50	75	0.5
	ImageNet	0.05	20	0.50	50	0.50	50	0.50	75	0.5
1000	FFHQ	0.00	100	0.25	500	0.10	500	0.10	500	0.25
	FFHQ	0.05	100	0.50	500	0.50	500	0.10	500	0.25
	ImageNet	0.05	100	0.50	750	0.50	500	0.10	750	0.50

Table S2. Hyperparameter values used for DDfire phase retrieval.

Operator	α_{shot}	# NFEs	K	δ_1
OSF	8	100	10	0.00
		800	20	0.00
CDP	45	100	10	0.00
		800	80	0.00

S2.4. Recovery methods

DDfire. Our Python/Pytorch codebase is a modification of the DPS codebase [8], and our code will be released upon the acceptance of this paper. For all but the runtime study in Fig. 6, we ran DDfire without an SVD and thus with the approximate renoising in (23). For the noiseless experiments, where the true $\gamma_w = \infty$, we set $\gamma_w = 10^6$ in DDfire. For η estimation, we approximate $\|\mathbf{A}\|_F^2$ using $\frac{1}{L} \sum_{l=1}^L \|\mathbf{A}\mathbf{w}_l\|^2$ with i.i.d. $\mathbf{w}_l \sim \mathcal{N}(\mathbf{0}, \mathbf{I})$ and $L = 25$. Table S1 shows the DDfire (K, δ_1) hyperparameters used for each linear inverse problem. Roughly speaking, $K \approx I_{\text{tot}}/2$ is a good choice for most problems, but $K \approx 1.5I_{\text{tot}}^{0.6}$ is better for inpainting. Reasonable choices for δ_1 are 0.25 in the noiseless case and 0.50 in the noisy case. To attain optimal performance on a given problem, one can tune (K, δ_1) via grid search. In all linear inverse problems we used $\eta_{\text{ddim}} = 1$, except at 20 NFEs where we used $\eta_{\text{ddim}} = 0.50$. For the phase retrieval experiments, we used $\eta_{\text{ddim}} = 0.85$ and the (K, δ_1) values listed in Table S2.

DDRM. We use the authors’ implementation from [25] with minor changes to work in our codebase.

DiffPIR. We use the authors’ implementation from [46] without modification. Hyperparameters were set according to the reported values in [45].

PIGDM. For the noiseless case, we use the IIGDM implementation from the authors’ repository [32] with minor changes to work in our codebase. For the noisy case, since the authors provide no implementation, we wrote our own IIGDM implementation that computed $(\mathbf{A}\mathbf{A}^H + \zeta_{t[k]}\mathbf{I})^{-1}$ using the efficient SVD implementation of \mathbf{A} from the DDRM codebase [25] on problems for which an SVD is available, and otherwise used CG.

DPS. For the linear inverse problems, we use the authors’ original implementation from [8] without modification. For all noisy problems, we use the suggested scale factors from [7, Sec. D.1]. For the noiseless problems, no suggested values were given in [7] and so we use grid search to find the LPIPS-minimizing DPS scale factor for each problem on a 100 image validation set. For box inpainting, we found the scale factor 2.0 to be optimal, and for all other problems, we found the scale factor 1.5 to be optimal.

For phase retrieval, we made minor adjustments to the DPS authors’ implementation to accommodate the likelihood $p_{y|z}(y|z) = \mathcal{N}(y; |z|, 1/\gamma_w)$ (used by all methods for fairness). We used grid-search to find the scale factor that minimized LPIPS on a 100-image validation set. The resulting values were 0.0075 for OSF and 0.05 for CDP.

DOLPH. As the DOLPH implementation is not publicly available, we implemented DOLPH in Python/PyTorch and used grid-search to find the step-size that minimized LPIPS on a 100-image validation set. The resulting step-sizes were 5×10^{-6} for OSF and 5×10^{-7} for CDP.

HIO. We translated the MATLAB implementation of HIO from [29] to Python and set the step-size parameter to 0.9. We then followed the runtime procedure described in [30]: For the OSF experiments, HIO is first run 50 times, for 50 iterations each, from a random initialization. The estimate $\hat{\mathbf{x}}$ with the lowest measurement residual $\|\mathbf{y} - |\mathbf{A}\hat{\mathbf{x}}|\|$

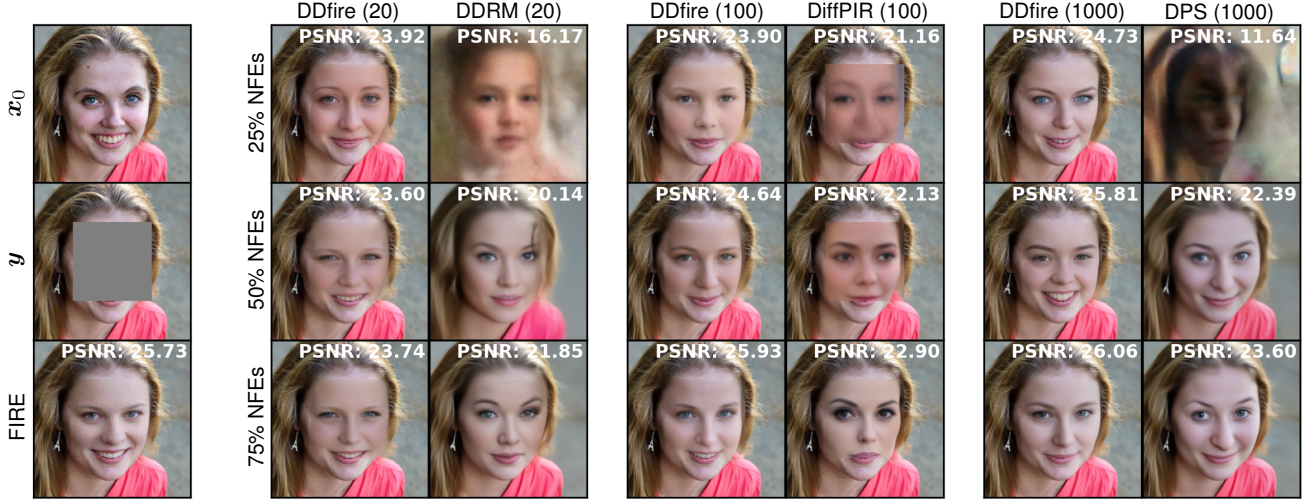


Figure S1. Left column: True x_0 , noiseless box-inpainting y , and 50-iteration FIRE approximation of $E\{x_0|y\}$. Other columns: Approximations of $E\{x_0|x_t, y\}$ at different t (as measured by % NFEs). Note the artifacts with DDRM, DiffPIR, and DPS.

is then used to reinitialize HIO, after which it is run for 1000 more iterations. Finally, the second and third color channels in the result are shifted and flipped as needed to best match the first color channel. For the CDP experiments, HIO is run once for 200 iterations from a random initialization.

prDeep. We used the Python implementation from [19]. As recommended by the authors of [30], we initialized prDeep with the HIO estimate for OSF experiments and with an all-ones initialization for CDP experiments. (Note that only prDeep uses the HIO initialization; DPS, DOLPH, and DDfire do not.) We tuned λ on a grid to minimize LPIPS on a 100-image validation set, which led to $\lambda = 0.1/\sqrt{\gamma_w}$ for OSF and $\lambda = 0.01/\sqrt{\gamma_w}$ for CDP.

S2.5. Compute

All experiments were run on a single NVIDIA A100 GPU with 80GB of memory. The runtime for each method on the GPU varies, as shown in Figure 6.

S3. Additional experimental results

Figure S1 shows typical approximations of $E\{x_0|x_t, y\}$ from the DDRM, DiffPIR, DPS, and DDfire solvers at different times in the reverse process for noiseless box inpainting, as well as PSNR of these approximations relative to the true x_0 . When approximating $E\{x_0|x_t, y\}$, PSNR is the appropriate quantitative metric because the exact $E\{x_0|x_t, y\}$ is the MMSE estimate of x_0 given x_t and y . The reconstructions from DDfire show some discontinuity across the masked and unmasked regions when the total NFE budget is small, but no severe artifacts. Also, the PSNRs of the DDfire approximations are uniformly higher

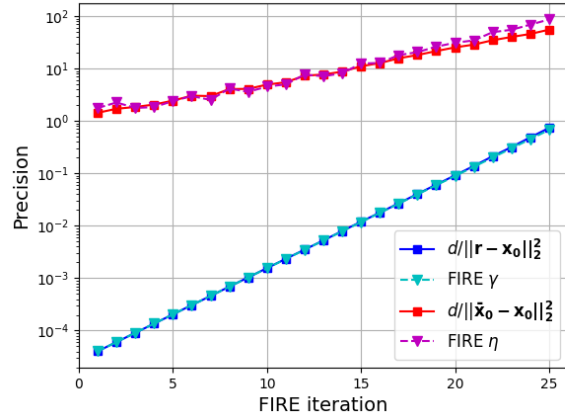


Figure S2. SLM-FIRE γ , true denoiser input precision $d/\|r - x_0\|_2^2$, SLM-FIRE η , and true denoiser output precision $d/\|\bar{x}_0 - x_0\|_2^2$ vs. SLM-FIRE iteration for noisy $4\times$ super-resolution at $t[k] = 1000$ for a single validation sample x_0 .

than those of the other approaches. Finally, the 50-iteration FIRE approximation of $E\{x_0|y\}$ (which is equivalent to $E\{x_0|x_T, y\}$ because x_T is non-informative) also shows no obvious artifacts.

Figure S2 shows SLM-FIRE's γ versus iteration i , for comparison to the true denoiser input precision $d/\|r - x_0\|_2^2$, and SLM-FIRE's η , for comparison to the true denoiser output precision $d/\|\bar{x}_0 - x_0\|_2^2$, for 25 FIRE iterations with $\rho = 1.5$ for noisy $4\times$ super-resolution at $t[k] = 1000$. We see that the SLM-FIRE estimates γ and η track the true precisions quite closely.

Figure S3 shows a similar figure for GLM-FIRE. In par-

Table S3. Noiseless FFHQ results.

# NFEs	Model	Inpaint (box)			Deblur (Gaussian)			Deblur (Motion)			4× Super-resolution		
		PSNR↑	LPIPS↓	FID↓	PSNR↑	LPIPS↓	FID↓	PSNR↑	LPIPS↓	FID↓	PSNR↑	LPIPS↓	FID↓
20	DiffPIR	22.42	0.1209	29.64	26.61	0.2627	34.62	36.24	0.1014	24.85	22.23	0.3598	47.37
	DDRM	22.25	0.1146	30.52	28.03	0.2365	35.91	-	-	-	29.83	0.1893	48.04
	DDfire (ours)	22.24	0.1097	29.24	31.26	0.1514	25.70	35.45	0.0814	23.01	28.84	0.1832	30.29
100	DiffPIR	22.79	0.1114	28.21	27.34	0.2344	28.38	36.69	0.0810	23.18	27.26	0.2378	30.12
	PIGDM	24.41	0.1118	28.35	28.33	0.2012	30.30	27.21	0.2368	38.91	29.46	0.1654	30.25
	DDfire (ours)	23.59	0.0909	26.33	31.39	0.1255	23.40	36.72	0.0626	22.20	28.93	0.1646	26.54
1000	DPS	21.09	0.1315	29.97	27.58	0.1833	24.32	31.49	0.1378	26.39	28.62	0.1742	28.74
	DDfire (ours)	24.69	0.0823	24.86	31.14	0.1252	23.27	36.76	0.0608	22.02	28.69	0.1633	24.61

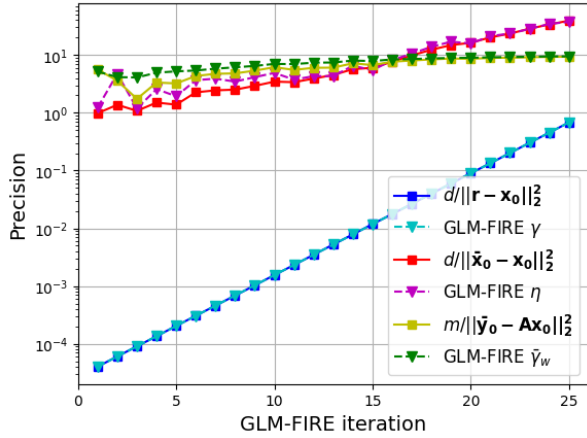


Figure S3. GLM-FIRE γ , true denoiser input precision $d/\|\mathbf{r} - \mathbf{x}_0\|_2^2$, GLM-FIRE η , and true denoiser output precision $d/\|\bar{\mathbf{x}}_0 - \mathbf{x}_0\|_2^2$, GLM-FIRE $\bar{\gamma}_w$, and noise precision $m/\|\bar{\mathbf{y}} - \mathbf{A}\mathbf{x}_0\|_2^2$ vs. GLM-FIRE iteration for noisy CDP phase retrieval at $t[k] = 1000$ for a single validation sample \mathbf{x}_0 .

ticular, it shows GLM-FIRE’s γ versus iteration i , for comparison to the true denoiser input precision $d/\|\mathbf{r} - \mathbf{x}_0\|_2^2$, GLM-FIRE’s η , for comparison to the true denoiser output precision $d/\|\bar{\mathbf{x}}_0 - \mathbf{x}_0\|_2^2$, and GLM-FIRE’s $\bar{\gamma}_w$, for comparison to the true pseudo-measurement precision $m/\|\bar{\mathbf{y}} - \mathbf{A}\mathbf{x}_0\|_2^2$ for noisy FFHQ phase retrieval at $t[k] = 1000$. We see that the GLM-FIRE estimates γ , η , and $\bar{\gamma}_w$ track the true precisions quite closely.

Table S3 shows the PSNR, LPIPS, and FID on a 1000-sample test set for the *noiseless* linear inverse problems under consideration (i.e., box inpainting, Gaussian deblurring, motion deblurring, and 4× super-resolution) and FFHQ images. For a fixed number of NFEs, DDfire outperforms all competitors in LPIPS and FID while also outperforming most competitors in PSNR. The best overall LPIPS/FID performance comes from DDfire at 1000 NFEs, with DDfire at 100 NFEs performing second best in most cases.

Example recoveries for noisy phase retrieval with FFHQ images are given in Figure S4.

Additional example recoveries for the noisy linear in-

verse problems with FFHQ images are shown in Figure S5.



Figure S4. Example recoveries from noisy phase retrieval with FFHQ images.



Figure S5. Example recoveries from noisy linear inverse problems with FFHQ images.